remote sensing

MDPI

Article

NDVI Analysis for Monitoring Land-Cover Evolution on Selected Deglaciated Areas in the Gran Paradiso Group (Italian Western Alps)

Simona Gennaro [1,†], Riccardo Cerrato [2,*,†], Maria Cristina Salvatore [1,2], Roberto Salzano [3], Rosamaria Salvatori [4] and Carlo Baroni [1,2]

[1] Institute of Geosciences and Earth Resources, National Research Council of Italy (IGG–CNR), Via G. Moruzzi 1, 56124 Pisa, Italy; simona.gennaro@igg.cnr.it (S.G.); mariacristina.salvatore@unipi.it (M.C.S.); carlo.baroni@unipi.it (C.B.)
[2] Earth Sciences Department, University of Pisa, Via S. Maria 53, 56126 Pisa, Italy
[3] Institute of Atmospheric Pollution Research, National Research Council of Italy (IIA–CNR), Via Madonna del Piano 10, 50019 Sesto Fiorentino, Italy; roberto.salzano@cnr.it
[4] Institute of Polar Sciences, National Research Council of Italy (ISP–CNR), Strada Provinciale 35d, 00010 Montelibretti, Italy; rosamaria.salvatori@cnr.it
* Correspondence: riccardo.cerrato@unipi.it
† These authors contributed equally to this work.

Abstract: The ongoing climate warming is affecting high-elevation areas, reducing the extent and the duration of glacier and snow covers, driving a widespread greening effect on the Alpine region. The impact assessment requires therefore the integration of the geomorphological context with altitudinal and ecological features of the study areas. The proposed approach introduces chronologically-constrained zones as geomorphological evidence for selecting deglaciated areas in the alpine and non-alpine belts. In the present study, the protected and low-anthropic-impacted areas of the Gran Paradiso Group (Italian Western Alps) were analysed using Landsat NDVI time series (1984–2022 CE). The obtained results highlighted a progressive greening even at a higher altitude, albeit not ubiquitous. The detected NDVI trends showed, moreover, how the local factors trigger the greening in low-elevation areas. Spectral reflectance showed a general decrease over time, evidencing the progressive colonisation of recently deglaciated surfaces. The results improved the discrimination between different greening rates in the deglaciated areas of the Alpine regions. The geomorphological-driven approach showed significant potential to support the comprehension of these processes, especially for fast-changing areas such as the high mountain regions.

Keywords: Landsat; spectral signature; Lateglacial; Egesen; Little Ice Age

Citation: Gennaro, S.; Cerrato, R.; Salvatore, M.C.; Salzano, R.; Salvatori, R.; Baroni, C. NDVI Analysis for Monitoring Land-Cover Evolution on Selected Deglaciated Areas in the Gran Paradiso Group (Italian Western Alps). *Remote Sens.* **2023**, *15*, 3847. https://doi.org/10.3390/rs15153847

Academic Editor: Gareth Rees

Received: 13 May 2023
Revised: 20 July 2023
Accepted: 27 July 2023
Published: 2 August 2023

1. Introduction

Anthropogenic global warming over the last few decades has been well documented [1–3] and mountainous regions are particularly sensitive to climate change [2,4,5]. This phenomenon is particularly intense in the European Alps, where significantly increasing temperatures were recorded with higher rates than the global average [6–8]. As a consequence, the European Alps are experiencing a decrease in snow and glacier covers associated with strong negative glacier mass balances [9], and for these reasons, the different sectors of the mountain range are becoming vulnerable to changes in the hydrological cycle [2,10]. In particular, climate variations affect the cryospheric components of the Alpine system and the induced glacier shrinkage causes responsible for the reduction of clear-water reservoirs [9]. Glaciers react to climate variations through changes in volume, extent and shape, and rising temperatures trigger the progressive reduction of the area covered by glacial bodies in mountainous regions [11–14].

In the Alpine range, the last major re-advancement phase of Holocene glaciers occurred during the Little Ice Age (LIA), which spanned chronologically between the mid-14th century and the mid-19th century [15–17]. Climatic conditions during the LIA presented a large regional variability, characterised by non-synchronous maximum glacier expansions across the European Alps [18–20]. Since the LIA, the early-21st century is witnessing a historically unprecedented glacier decline led by the ongoing global warming, which is affecting the entire planet [21]. The response of the morphoclimatic system to climate change and warming produced a significant landscape change, shifting from a glacial to a periglacial environment, characterised by alpine and subalpine ecosystems and their related ecotones. The retreat of glaciers creates new areas available for colonisation by biota successions [22]. Indeed, this process was already active in the past with different rates than those active in the present time, highlighting an acceleration of the greening process in the last few decades [22–25].

Land cover is a primary essential climate variable, since it regulates water and energy exchanges with the atmosphere [26]; thus, the evolution of land-cover conditions in terms of seasonality and spatial distributions are strictly linked to regional climatic conditions. Changes in cover can be caused by climate change at a regional scale as well as by human activities [27]. Considering the Alpine deglaciated areas, the land-cover types include cryospheric end-members (snow and ice), bare rocks (function of local conditions), pioneer flora (lichens and mosses), and climax communities (grass and low shrubs). The impact of climate change is expected to drive the evolution under this sequence and succession [28].

The primary target of this process is the energy budget of the involved areas, since the snow cover features the highest capacity to reflect sunlight in the whole spectral range, generally defined as broadband albedo (ρ_{bb}). The ice and snow reflectance values are generally high ($0.7 < \rho_{bb} < 0.9$), whereas the exposure of ice in glaciated bodies differs from this range due to its lower reflective feature in the shortwave infrared domain ($0.5 < \rho_{bb} < 0.7$). In the occurrence of rocks not being covered by snow and ice, the optical behaviour is heavily impacted. In fact, rocks have low reflectance in the visible range and in the shortwave infrared ($\rho_{bb} < 0.5$). Finally, where vegetation starts to develop, the albedo strongly decreases ($\rho_{bb} < 0.3$) and the solar radiation is absorbed even more in the visible and shortwave infrared wavelength domains, leaving a specific reflectance feature in the near-infrared spectral region (700–900 nm). The optical behaviour of the above-mentioned land-cover types offers the opportunity to detect this evolution by using remotely sensed observations. The spectral feature characterised by the occurrence of vegetation is, in fact, the so-called 'red edge', which is identified by the Normalised Difference Vegetation Index (NDVI), and can be used to quantify vegetation greenness. The NDVI is also useful for understanding vegetation density and assessing health changes in plants. Despite the NDVI being largely used to monitor forested areas and land-cover changes by generally using a coarse spatial resolution (based on the MODIS instrument) [29–34], few studies are now focused on the use of NDVI obtained with a higher spatial resolution for monitoring variations of vegetation over time and to assess changes in deglaciated areas [22,28,35].

This study presents the analysis of NDVI time series that were selected in protected, natural, and scarcely-populated areas, located in the Italian Western Alps. Here, the deglaciation onset is a well-established time reference, and the NDVI analysis on trends was focused on characterising the non-alpine and alpine ecosystems. Particular attention was devoted to their associated ecotones in both past- and recently deglaciated areas. Further effort was focused on assessing variations of the optical behaviour in the deglaciated area in relation to the recent warming.

2. Study Area

The study area is located in the Gran Paradiso Group (Graian Alps; 45.40–45.75°N 7.01–7.60°E; Figure 1), belonging to the Northwestern Alps according to the International Standardised Mountain Subdivision of the Alps (ISMSA-SOIUSA; [36]). The Gran Paradiso is the highest peak (4061 m a.s.l.) in the study area, which was limited northerly by the

Dora Bàltea river and southerly by the Torrente Orco. The region includes the valleys of Rhêmes, Valsavarenche, Cogne, and the northern sector of the Orco catchment.

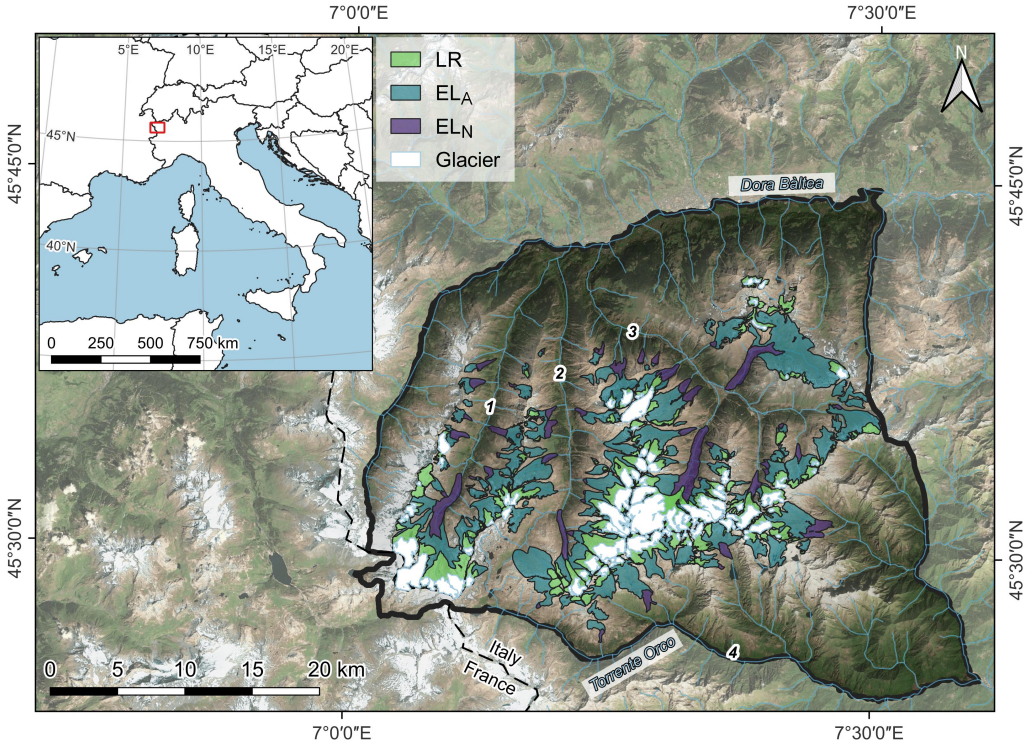

Figure 1. Location map of the study area. The thick solid black line represents the study area; thin dashed black lines represent the Italian national border; the solid red line in the inset represents the main map's footprint. Glaciers outlines at 1989 CE modified after [37–39]. Key: 1: Rhêmes valley; 2: Valsavarenche; 3: Cogne valley; 4: Orco valley. LR: LIA–Recent; EL$_A$: Egesen–LIA (alpine); EL$_N$: Egesen–LIA (non-alpine). Basemap: Microsoft™ Bing.

The Gran Paradiso Group represents an internal crystalline massif that outcrops in the Italian Western Alps (Pennidic Domain); it is a tectonic window surrounded by units that derive from the Ligure-Piemontese ocean basin [40–43]. The area is mainly characterised by the presence of crystalline lithotypes, in particular by Permian augen gneiss and meta-granites, deriving from porphyritic granitoids, intruded into a polymetamorphic unit characterised by fine-grained gneiss, paragneiss and micaschists. Oceanic and ophiolite Mesozoic units are composed by Cretaceous calcschists, micaschists, black phyllite, and by Jurassic foliated and massive prasinite, meta-basalt, amphibolite, and serpentinite [44–47].

The area retains the morphology inherited by the Pleistocene and Holocene glacial activities, characterised by a typical Alpine landscape with erosional and depositional landforms (U-shaped valleys, glacial cirques, horns, arêtes, trimlines, moraines, blockfield, etc.) [48]. Glacial deposits are, in fact, rife in the area [37,48]. Older glacial moraines were dated by applying the ^{10}Be Surface Exposure Dating, which furnished an age related to the regional Egesen stadial *Auct.* [37]. Well-shaped moraines, characterised by sharp ridges and a sparser vegetation cover compared to the older glacial moraines, testify the most advanced position reached by glaciers in the Holocene during the LIA [20,37]. Nowadays, 72 glaciers exist in the area, extending for about 37 km^2, making the Gran Paradiso Group one of the most glacierised massifs of the Italian Northwestern Alps [38].

According to the Köppen–Geiger climate types, climatic conditions in the selected area are classified as continental (i.e., absence of dry season with warm or cold summers, Dfb or Dfc) or as polar tundra (ET), depending on the geographic location and altitude [49,50]. Precipitations are scarce compared to the Italian Eastern Alps [51–53] with a range between 480 mm year^{-1} for valley floors and 1400 mm year^{-1} in the valleys' head [7,54,55]. Mean

temperatures in the 1961–1990 period range from −6.4 °C in January to 9.2 °C in July, with an annual mean of 0.9 °C. However, in the 1991–2020 period mean temperatures range from −5.3 °C in January to 10.5 °C in July, with an annual mean of 1.9 °C (CRU TS 4.06 cell centre 45.75°N, 7.25°E, accessed 4 July 2023) [56].

The ecological context of the study area is characterised by a primary succession, with pioneer species (lichens) colonising the recently exposed rocks, followed by vascular plants, shrubs, and trees. This phase ranges from the early- to the mid-stages, depending on the post-deglaciation exposure length of rocks in terms of time, altitude, topography, and water availability [57]. The region of interest is mostly covered by alpine grassland, which includes three vegetation subtypes: natural, sparsely vegetated (on rocks, scree, or gravel), and wet grasslands [58,59]. Despite the fact that species assemblages are generally representative of alpine grasslands, the different valleys have local dominance and abundance patterns, for the different vegetation subtypes [58]. While pure grasslands are dominated by *Nardus* (L.), *Trifolium* (L.) and *Carex* (L.) genus, wetlands are dominated by *Nardus*, *Carex*, *Salix* (L.) and mosses. The dominating species in the rocky subtype belong to the *Silene* (L.), *Festuca* (L.), *Salix*, and *Plantago* (L.) genus [58]. Concerning non-alpine vegetation, the lower elevations extending to the sub-alpine belt are characterised by coniferous forests (CLC90 level 3 classes 3.1.2), composed by various associations of *Pinus sylvestris* L., *Picea abies* (L.) H.Karst., *Pinus cembra* L., and *Larix decidua* Mill. Above the coniferous forests, the landscape shows shrub and/or herbaceous associations (CLC90 level 2 class 3.2), dominated by *Alnus viridis* (Chaix) DC., *Juniperus communis* L., *Juniperus communis var. saxatilis* Pall., *Calluna vulgaris* (L.) Hill, *Rhododendron ferrugineum* L., and *Vaccinium myrtillus* L.

3. Materials and Methods

3.1. Datasets

We selected deglaciated areas bracketed by key glacial advances that have occurred since the Lateglacial Period: the first deglaciated area comprised between the Egesen moraines, depicting the last Lateglacial advance, and the LIA moraines, which outline the Holocene most advanced glaciers' position (EL here hence; ranging in age between 13.8 ± 0.8 ka–1820 CE in the area) [37,60]. The second deglaciated area extends between the LIA maximum positions and the 1989 CE glaciers' limits (henceforth referred to as LR). The 1989 CE is the closest glacier snapshot since the launch of Landsat 4, which took place 16 July 1982. The Egesen and LIA glaciers outlines were derived from [37], while the 1989 CE glacial limits were manually digitalised from orthophotos available from web map services (WMS) provided by the 'Portale Cartografico Nazionale' [61,62].

The deglaciated areas pertaining to the above-mentioned time range were obtained by combining the different polygon vector files and by defining additional and geomorphologically driven areas of interest. The defined polygons were then filtered excluding those with an extent smaller than 900 m^2. In addition, polygons associated with the Egesen–LIA range were further divided using the ecosystems' classification [63], creating two sets of polygons respectively identified as Egesen–LIA non-alpine (EL_N, hence here) and Egesen–LIA alpine (EL_A) (Figure 1, Table 1). Finally, the optimisation of the processing time was obtained by converting vector data of deglaciated areas to raster grids with the Landsat spatial resolution.

The CORINE Land Cover raster dataset referring to the 1986–1998 time period (CLC90, hence here; https://land.copernicus.eu/pan-european/corine-land-cover/clc-1990?tab=mapview, accessed 20 January 2023) was resampled with the satellite product spatial resolution (i.e., pixel size xy: 30 m). This raster layer was used to tag satellite pixels with the associated land cover class (see Sections 3.2 and 3.4).

Table 1. Deglaciated belt summary.

	Time Span	Ecosystem Belt [1]	Total Area [km^2]	Elevation Median [m]	Elevation Range [2] [m]
EL_N	Egesen–LIA (13.8 ± 0.8 ka–1820 CE ca.)	non-alpine	29.38	2183	1742 2359
EL_A	Egesen–LIA (13.8 ± 0.8 ka–1820 CE ca.)	alpine	142.86	2680	2407 3036
LR	LIA–Recent (~1820–1989 CE)	alpine	67.21	2866	2380 3248

[1] following [63]. [2] minimum and maximum elevation range are here intended as 5th and 95th percentile of the pixel elevation distribution.

3.2. Satellite Data

Among several Earth Observation missions, the Landsat Program provides the longest image time series since the first platform was launched in 1972 [29], even if the spatial and spectral resolution of the first satellites were coarse. The launch of the Landsat 4 in 1982, equipped with the Thematic Mapper (TM) instrument, represented a significant improvement in terms of spatial and spectral image resolutions. The program continued with the same instrument onboard the Landsat 5 (launched in 1984) and with a new sensor, the Operational Land Imager (OLI) instrument, deployed on the Landsat 8 and 9 (launched in 2013 and 2021, respectively). This study considered the Landsat 4, 5, 8, and 9 platforms, with particular attention to the product collection 2 at the Level 2 processing. Scenes (path: 195; row: 28) with values of the bottom-of-atmosphere surface reflectance cover the last portion of the ablation season (i.e., July–September) of the 1984–2022 period. Data were filtered considering the cloud coverage. Thus, scenes with cloudiness lower than 20% in the study area were selected and the computational time was reduced by cropping scenes using the area of interest. The NDVI values were calculated according to Equation (1):

$$NDVI = \frac{\rho_{NIR} - \rho_{RED}}{\rho_{NIR} + \rho_{RED}} \quad (1)$$

This index was introduced by [64,65] and it estimates the difference between the near-infrared reflectance (ρ_{NIR}) and the red reflectance (ρ_{RED}). These radiative features are influenced both by the presence of chlorophyll, which absorbs the photosynthetic active radiation (400–700 nm), and by the vegetation functionality (leaf area, biomass, phenology, etc). The NDVI value ranges from $+1$ to -1, and shows negative values in the occurrence of water, soil, snow, and man-made surfaces. Vegetated areas, on the other hand, have positive values between 0.2 and 1. Dense vegetation canopy always has a value higher than 0.5, while sparse vegetation such as shrubs and grasslands or senescent crops can vary between 0.2 and 0.4.

The Regions Of Interest (ROIs) include pixels belonging to the defined deglaciated areas (LR, EL_A, and EL_N). The ROI pixels were differentiated using the quality assurance layer. Pixels classified as "Clear with lows set" were selected (i.e., quality assurance layer pixel value = 5440 for Landsat 4 and 5, and pixel value = 21824 for Landsat 8 and 9). The whole dataset was subset in terms of each calendar year, only considering the late-summer season. Each summer season subset was analysed pixel-by-pixel, looking for the NDVI maximum producing the NDVI-maxima on a yearly basis (called 'yearly scene', here hence). This process homogenises the NDVI, retaining the values related to the peak of the vegetation period, independent from the ground's first snow-free calendar date, while the use of the median tends to flatten the differences among them [30]. Moreover, the advantage of adopting this procedure is the reduction of discarded pixels (e.g., cloud-covered pixels in one scene), thus increasing the statistical significance of each yearly scene.

3.3. Spectral Libraries

The identification of the spectral endmembers (Figure 2a) was approached considering different spectral measurements in the visible and shortwave infrared domain (400–2500 nm) available in the literature. We considered the ECOSTRESS library [66,67] for rocks and vegetation species, the SISpec collection [68] for snow and ice, the SpecLib catalogue for lichens observations [69] and the ECOSiS collection for moss measurements [70]. The selected vegetation species and rock types were identified considering the descriptions presented in Section 2. Further improvements will be possible with future ground-based surveys aimed at developing a specific spectral library for the study area.

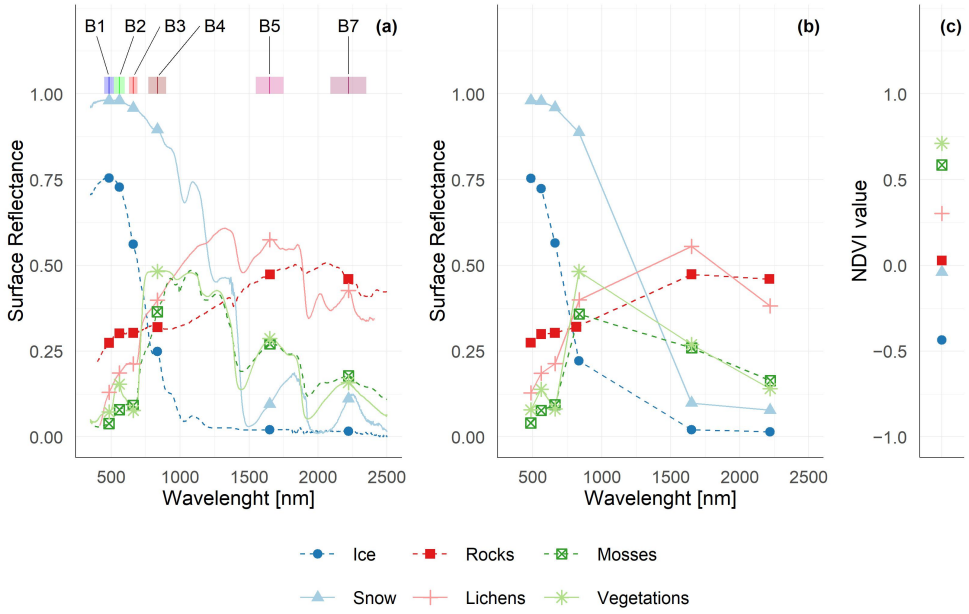

Figure 2. (**a**) Spectral endmembers identified using observations available in the literature. (**b**) Landsat 5 TM resampling of spectral endmembers identified using observations available in the literature. (**c**) NDVI value for the selected spectral endmembers. To be noted the different vertical scale.

3.4. Statistical Analysis

The classification of the NDVI values extracted by each yearly scene was based on the criteria of elevation, slope, and aspect. This procedure allows grouping pixels with matching physical properties (i.e., elevation, slope, and aspect), in order to evaluate the influence of such parameters on the final NDVI. Geomorphological information was obtained from the European Digital Elevation Model (EU-DEM), version 1.1 tile E40N20 (https://land.copernicus.eu/imagery-in-situ/eu-dem/eu-dem-v1.1, accessed 4 January 2023). The original EU-DEM spatial resolution of 25 m, with a vertical accuracy of ±7 m, was resampled to homogenise its datum and spatial resolution to those of the other raster data used in this study (UTM WGS84, pixel size xy: 30 m).

Non-parametric Mann–Kendall and Theil–Sen slope tests were used to assess the presence of a monotonic trend and its magnitude in the time-series. Non-parametric tests were preferred, since the entire data of the time series does not show normality and stationarity, according to Anderson–Darling and Kolmogorov–Smirnov normality tests. Although normality and stationarity are fundamental assumptions for parametric tests, under non-normality conditions the non-parametric tests offer higher statistical power and robustness than parametric tests [71,72]. Mann–Kendall Tau, Sen's slope, and their

respective p-values were considered and evaluated, and the difference between slopes were assessed by means of Equation (2) [73]:

$$z = \frac{\beta_1 - \beta_2}{\sqrt{SE\beta_1^2 + SE\beta_2^2}} \quad (2)$$

where β_1 and β_2 are the Sen's slope index of the considered time series and SE their standard error.

The spectrum for each yearly scene was calculated considering the median of the pixels belonging to each satellite band. Non-parametric Kruskal–Wallis tests were used to check if the difference between each band of the considered pair of spectra is significant. To limit the high-frequency effect of the time series on the tests, data belonging to the decades of 1990–1999 and 2013–2022 have been grouped. Moreover, the existing differences between couples of spectra were evaluated using the spectral contrast angle (θ; [74]), defined as:

$$\cos\theta = \frac{\sum_{i=1}^{n} a_i\, b_i}{\sqrt{\sum_{i=1}^{n} a_i^2\ \sum_{i=1}^{n} b_i^2}} \quad (3)$$

where a_i and b_i are the surface reflectance value at band i for median spectra a and b. Following Equation (3), a multi-dimensional space was simplified to a bi-dimensional space, where the spectra are characterised by a vector. Similar spectra, independent of their intensities, are characterised by similar vectors in this new bi-dimensional space and, consequently, a low θ exists between them. This condition implies a $\cos\theta$ near to 1. Conversely, dissimilar spectra are characterised by a θ of 90°at maximum, thus implying a $\cos\theta$ equal to 0.

All computations were performed using the R project 4.2.1 software [75], raster (v. 3.5-21, https://CRAN.R-project.org/package=raster, accessed on 29 July 2023), nortest (v. 1.0-4, https://CRAN.R-project.org/package=nortest, accessed on 29 July 2023), and trends (v. 1.1.4, https://CRAN.R-project.org/package=trend, accessed on 29 July 2023) packages.

4. Results

The analysed dataset included a total of 83 scenes available for the period 1984–2022 CE; in each scene, data were cropped using an ensemble ROI area of 262,457 pixels. Satellite data were available for each year except for 1987, 2002, 2005, 2007, and 2012 CE (Figure 3). The cloud coverage, despite considering a selection of mostly clear-sky images, caused a decrease of the available pixel count from a minimum of 9.67% in 2022 CE, to a maximum of 75.33% in 1986 (μ = 36.51%, median = 30.72%, σ = 19.13%). The available pixel count grouped by year and aspect spanned from a minimum of 4.27% of the ROIs pixels facing southward in 1986 CE, to a maximum of 26.24% of the ROIs pixels facing westward in 2022 CE. The slope-oriented analysis showed that pixel distributions were non-normal, being mainly platykurtic and negatively skewed (i.e., a higher number of pixels characterised by low slope values). Finally, each deglaciated ROI was considered and the number of pixels was analysed in terms of aspect, showing that the minimum number of considered pixels is 0.05% of ROI pixels for LR facing southward in 1995 CE, whereas the maximum number is 17.37% of ROI pixels for EL_A facing westward in 2022 CE.

The NDVI time series were built considering all the pixels available in each yearly scene, grouped by ROIs and aspect, and the obtained median values showed different means and trends among the considered deglaciated areas. Pixels belonging to EL_N returned higher values than those belonging to EL_A time-series, but both had a comparable trend. The highest NDVI median values were detected since 2013 CE on eastward-facing pixels associated with the EL_N deglaciated area. Regarding the recently deglaciated area (i.e., LR), pixels always showed low NDVI median values with no significant trends, with the exception of the southward-facing pixels (Figure 3; Table 2). Despite this, EL_N area resulted in the steepest trend slope followed by EL_A and LR (Table 2).

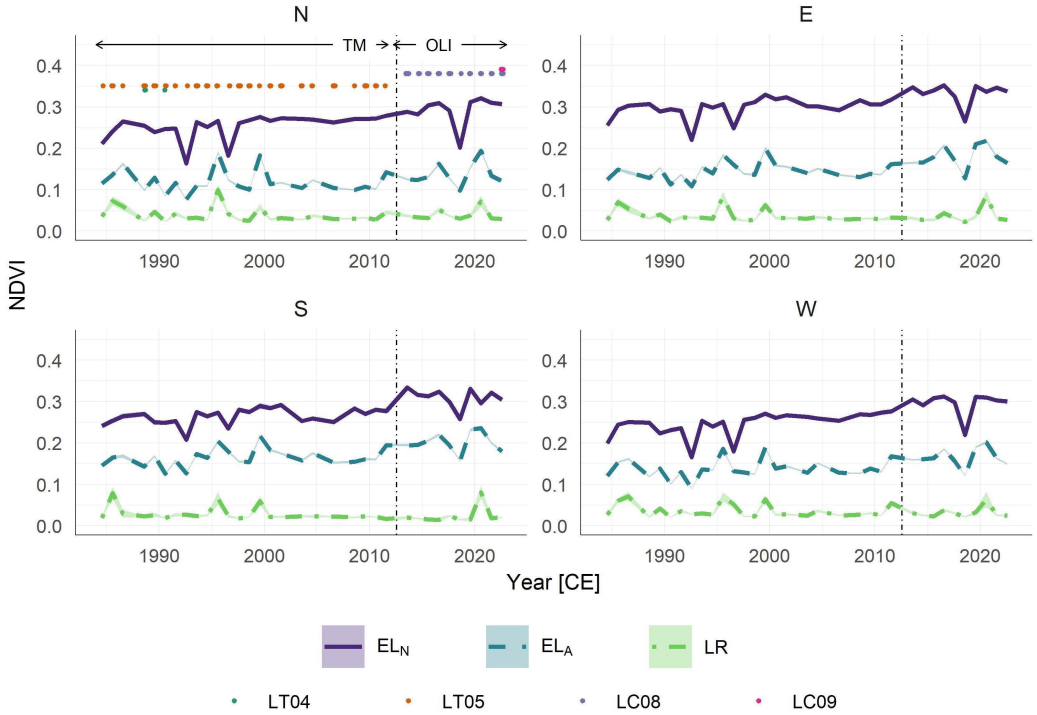

Figure 3. NDVI time series grouped by aspect and deglaciated area. Shaded areas around the lines identify the confident interval of the pixel distribution ($\alpha = 0.001$); dots on the top-left facet identify the used scenes; the vertical line identifies the passage from the Thematic Mapper (TM) to the Operational Land Imager (OLI).

Table 2. Mann–Kendall test Tau (τ) and Sens slope (S; reported as 10^{-3}) values.

	EL_N		EL_A		LR [1]	
	τ	S	τ	S	τ	S
N	0.665	2.15	0.155 *	0.62 *	−0.143 *	−0.18 *
E	0.519	1.73	0.390 †	1.39 †	−0.039 *	−0.04 *
S	0.515	2.11	0.412	1.54	−0.365 †	−0.28 †
W	0.658	2.61	0.326 †	1.31 †	−0.015 *	−0.03 *

[1] Mann–Kendall and Sens slope tests were performed on the 1990–2022 time period. * identifies value not significant at $\alpha = 0.05$ level. † identifies value not significant at $\alpha = 0.001$ level.

Further analyses were approached reducing the complexity of the considered datasets, subsetting pixels considering different criteria based on ROIs, slope, elevation, and land-cover class (CLC90 at level 2). The aim of this additional step was the reduction of interference related to topographic or pedological factors, which cause critical issues in the NDVI analysis. More precisely, we only considered pixels characterised by a slope of less than 30°, belonging to two elevation ranges (i.e., 2400–2600 m a.s.l. and 2800–3000 m a.s.l.), and land-cover classes associated with open spaces with little or no vegetation (i.e., bare rocks and sparsely vegetated areas identified by CLC90 level 3 classes 3.3.2 and 3.3.3, respectively). The selection of the open spaces with little or no vegetation (CLC90 3.3), removed the contribution of artificial surfaces (CLC90 1) and agricultural areas (CLC90 2), which were present especially in the EL_N ROI. Consequently, the subset criteria also limited the influence of well-developed vegetation, which is identified as forest occurring especially in EL_N (CLC90 3.1), and shrubs and/or herbaceous vegetation associations (CLC90 3.2), present significantly in the EL_A ROI, and scarcely in the LR ROI. The CLC90 3.3 criteria enhanced, in conclusion, the selection of common land-cover classes present in the three deglaciated ROIs (Figure S1 in Supplementary Material to compare the number of considered pixels), excluding from the analysis those areas characterised by well-developed vegetation (CLC 90 3.1) or by grassland (CLC 3.2) that are not common to all the interested

ROIs. To avoid excessive fragmentation of the dataset, and thus less robust statistics, the following analysis were performed on the selected pixels not grouped by their aspect.

Considering only the selected pixels, the NDVI values were comprised between −0.01 and 0.27, and, therefore, comparable with the NDVI values of the CLC90 class to which they belong (bare rocks and sparsely vegetated areas). Moreover, significant monotonic trends in NDVI values were visible in all the categories (Figure 4; Table 3), except for bare rocks occurring at any considered elevation range in EL_N and only at the 2800–3000 m a.s.l. elevation range in LR. The NDVI time series derived from the 2400–2600 m a.s.l. bare rock EL_A and LR, and sparsely vegetated areas' LR pixels showed a breaking point in the trend in the 2011 CE, with the most recent portion reporting a slope of NDVI values from 74% to 364% steeper than the pre-2011 CE portion (Figure 4).

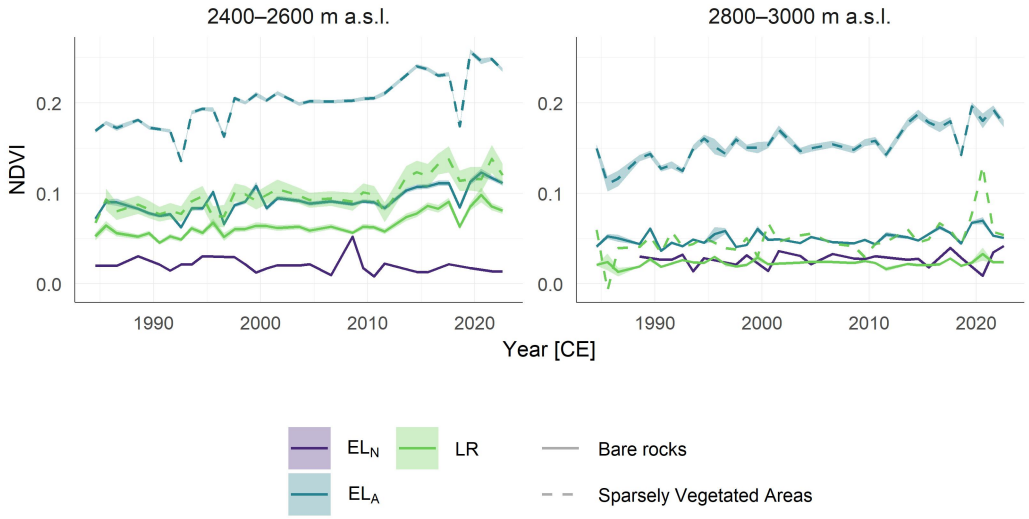

Figure 4. NDVI time series of pixels located at 2400–2600 m a.s.l. and 2800–3000 m a.s.l. elevation ranges characterised by bare rocks and sparsely vegetated areas CLC90 classes. Shaded area around lines identifies a confident interval of the pixels distribution ($\alpha = 0.001$) for time series characterised by at least 50 pixels.

Table 3. Mann–Kendall test Tau (τ) and Sens slope (S; reported as 10^{-3}) values of selected pixels.

Elevation Class (m a.s.l.)	CLC90 Class	EL_N		EL_A		LR [1]	
		τ	S	τ	S	τ	S
2400–2600	3.3.2	−0.212 *	−0.30 *	0.565	1.16	0.591	1.27
	3.3.3	–	–	0.668	2.34	0.586	1.70
2800–3000	3.3.2	0.138 *	0.14 *	0.269 †	0.34 †	0.044 *	0.03 *
	3.3.3	–	–	0.572	1.74	0.328 †	0.68 †

[1] Mann–Kendall and Sens slope tests were performed on the 1990–2022 CE time period. * identifies value not significant at $\alpha = 0.05$ level. † identifies value not significant at $\alpha = 0.001$ level.

The comparison of trends evidenced that, subsequent to the 1989 CE, the NDVI of EL_A's sparsely vegetated areas increased significantly faster ($\alpha < 0.05$) than the NDVI of bare rock areas, at both elevation levels considered. Conversely, the NDVI of LR sparsely vegetated areas increased significantly faster than the NDVI of EL_N bare rocks areas within a 2400–2600 m a.s.l. elevation range. It also increased faster than the NDVI of LR bare rock areas at 2800–3000 m a.s.l. elevation range. Comparing the time series' slope among elevation ranges, it was found that bare rock areas' NDVI time series are always steeper ($\alpha < 0.05$) within a 2400–2600 m a.s.l. than within a 2800–3000 m a.s.l. elevation range except for the EL_N 2400–2600 m a.s.l. time series that showed a negative slope even if not significant. Regarding the sparsely vegetated NDVI time series, the only significant

difference in trend ($\alpha < 0.05$) was observed between LR 2800–3000 m a.s.l. NDVI time series and both EL_A and LR 2400–2600 m a.s.l. NDVI time series, with the former showing a flatter slope (Figure 4).

The spectra obtained by the considered classes showed that bare rock EL_A and LR at both considered elevation ranges were comparable among them, as well as the spectra obtained for EL_A sparsely vegetated areas at both elevation ranges and those obtained for LR at 2400–2600 m a.s.l. Other similar spectra were those obtained for EL_N and those obtained for the LR sparsely vegetated areas at 2800–3000 m a.s.l. (Figure 5).

The Kruskal–Wallis test was used to compare similar distributions to highlight significant difference between the median of two distributions (Figure S2 in Supplementary Material). Each single deglaciated areas and land cover classes were analysed separately in terms of time ranges (1990–1999 CE against 2013–2022 CE). The cross-comparison of decades distributions was only possible for bare rocks in EL_A and LR (Figure S2 in Supplementary Material).

All tests returned remarkable results ($\alpha = 0.001$), indicating that a difference existed in all the cases considered between the 1990–1999 CE and the 2013–2022 CE spectra. However, the contrast angle distances between the spectra always return θ lower than 1 degree, denoting high similarities in the considered spectra, despite their significant distance.

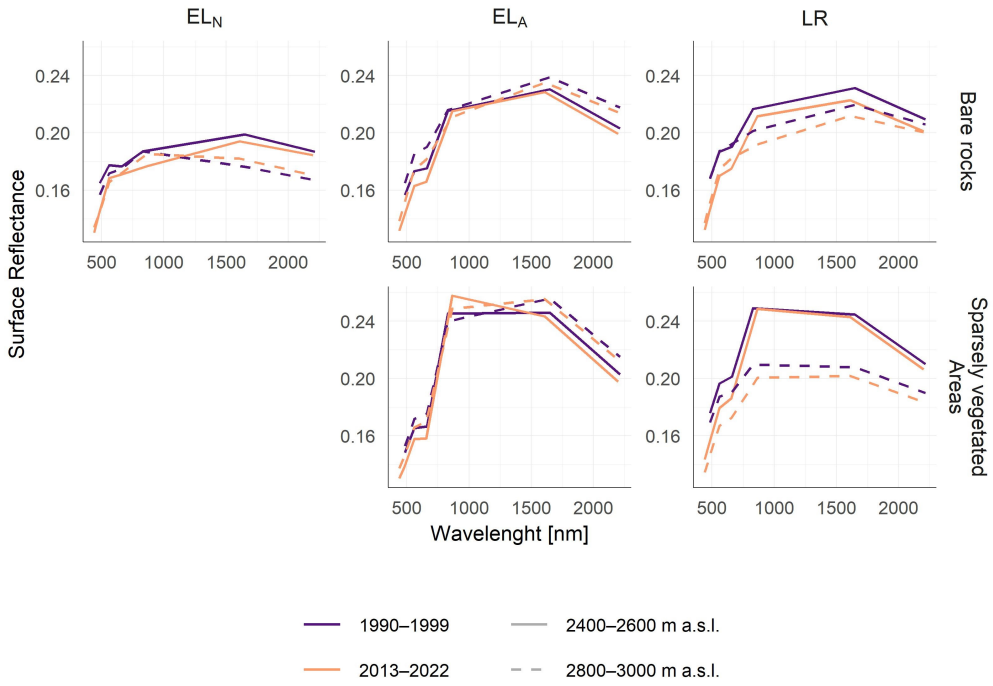

Figure 5. Median spectra for 1990–1999 CE and 2013–2022 CE decades at 2400–2600 m a.s.l. and 2800–3000 m a.s.l. elevation ranges characterised by bare rocks or sparsely vegetated areas.

5. Discussion

The entire dataset, which includes all the land-cover classes described in the CLC90, highlighted that the difference between the EL_N and the EL_A NDVI, equal to 0.127 ± 0.096 (Figure 3), was strongly influenced by the fractional composition of land-cover classes in the different ROIs. The large variability observed in the whole dataset is explained by pixels identified as forests (CLC90 3.1) and as shrub and/or herbaceous associations (CLC90 3.2) (Figure S1 in Supplementary Material). In fact, these classes, being representative of the already developed association and not of pioneer species, impact on trends observed for the different ROIs, having different reaction times, in terms of greening, to climate change. The selection of pixels with low and sparse vegetation (CLC90 3.3) was the most reliable approach for assessing the greening process in the selected area of interest. Filtering the CLC90 classes, NDVI resulted in trends with the lowest slopes of -0.30×10^{-3} year^{-1}, obtained for bare-rock areas (CLC90 3.3.2) located in EL_N at 2400–2600 m a.s.l. The highest trend slope was

2.34×10^{-3} year^{-1}, obtained for sparsely vegetated areas (CLC90 3.3.3) located in EL_A at 2400–2600 m a.s.l. (Table 3). These values depicted a different environmental condition from the one inferred by the whole dataset (compare Figures 3 and 4). In fact, both forests and shrubs and/or herbaceous associations were characterised by higher NDVI values than the bare rocks and sparsely vegetated areas classes, implying a higher median in pixels grouped by aspect and not by elevation range and land cover. Moreover, the LR ROI offered the opportunity to further simplify the framework, isolating the aspect contribution in the absence of altitude and land-cover related variability. Although LR NDVI values grouped by aspect showed negligible trends (Figure 3, Table 2), pixels characterised only by sparse vegetation evidenced the presence of a significant NDVI trend (Figure 4, Table 3). Thus, specific information for land cover change in the study area was obtained by filtering the pixels based on each land-cover class, elevation, and deglaciated area. These results were supported by the different Sens slope values performed on the different considered pixel groups (Table 2). The aspect-oriented analysis was unfortunately limited by statistical issues related to the limited pixel number.

Considering the pixels filtered by their elevation and land-cover classes, the starting NDVI values described land-cover types characterised by loosely developed vegetation for most of the ROIs (compare Figures 5 and 2b). Additional descriptions about the vegetation associations were not possible, since the spatial resolution and the spectral mixing issue impact on the pixel spectral signature. The spatial resolution of Landsat data constrained the study, as well as the lack of specific spectral libraries for the study area. The Landsat-derived spectra (Figure 5) highlighted, in fact, a mixed pixel issue, which affected the fractional composition at a 30 m pixel resolution. Further interpretation of the land cover composition requires a specific spectral unmixing analysis that will be possible in the future with the development of in situ spectral libraries. Longer time-series will be, moreover, potentially available when sensors with higher spatial resolution will be included. On the other hand, only a qualitative recognition was possible with the analysis of the spectral similarity between pixels, belonging to bare rocks (CLC90 3.3.2), and signatures, available in spectral libraries, for lichens and rocks (compare Figures 5 and 2b). Similar affinities were identified between pixels associated with sparsely vegetated areas (CLC90 3.3.3) and spectral signatures, which are potentially produced by a mixture of mosses–grasses and lichens–rocks. The rock weathering, the soil moisture content, and even the vegetation variability represented a limit for a more quantitative determination at this stage of the study. Nonetheless, NDVI values were used to assess the vegetal biomass in relation to deglaciation and altitude. The trend analysis confirmed the statistical significance of the observed increments, which can be associated with the biomass accumulation, coherently with a general lowering of surface reflectance in 2013–2022 CE compared to the 1990–1999 CE time periods (Figure 5). The detected evolution was consistent with the regional observations reported for the Northwestern Alps [76], the French Western Alps [33], the Austrian Northeastern Alps [22], the Eastern Alps [35], and more in general for the European Alps [34]. Rock weathering processes and other external factors (biotic and/or abiotic) were the possible drivers of NDVI negative trends showed by bare rocks areas located in EL_N at low altitudes. Both components limited the development of the pioneering stage of floral successions. Especially in the last few years, the detected increase of biomass was not confirmed by CORINE datasets, since they did not report significant changes in pixel classification in the last two published versions (i.e., CLC 2012 and 2018; Figures S3 and S4 in Supplementary Materials). Although an increase of pixels classified as vegetated areas was observed in the first datasets (CLC 2000 and 2006), it is relevant to notice a meaningful change in the spatial resolution of the CORINE products. Nevertheless, further analyses are required to assess such variations to real land-cover changes concerning the satellite sensors used by the different CORINE products. In addition, further analyses are required for land-cover changes, involving more spatially resolved investigations, to better understand the NDVI negative trend in the study area. This novel information will

be relevant especially in the framework of the hydrological and the geomorphological settings of the European Alps [25,34,77].

The snow cover dynamics represent an additional key driver for the greening processes [78]. The analysis of the snow-related index was, in fact, already performed by [55] on the same satellite product collection over the considered time window (1984–2022 CE). The time series related to the Snow Cover Extent (SCE) showed negligible trends and outliers between winter 1984 and 2017 CE for the study area [55]. Comparing this snow-related dataset to the presented NDVI time series, the negative NDVI outlier detected in 1991 CE (Figure 4) can be related to climatic anomalies that occurred during the vegetative season. Further specific analyses will be required to investigate such anomalies as well as the additional 2018 outlier, when few satellite data were available (i.e., only one scene was processed due to cloud-cover limitations in 2018). The picture of the greening evolution during the last few decades will be enhanced in the future using additional spectral indexes (e.g., Normalized Difference Snow Index), focused on describing more precise SCE timing from Landsat and/or other Earth Observation missions. The support from further data sources, such as meteorological time series (both measured and/or synthetic [51,54]), will provide key information identifying the drivers impacting on NDVI trends, their breaking points and outliers (Figure 4) [32].

The proposed approach, based on the geomorphological-driven selection of deglaciated areas, supported the characterisation of the behaviour of vegetation in colonising newly formed surfaces in the alpine and non-alpine belts. This approach provided relevant information in both recently-deglaciated and fast-changing areas, and past-deglaciated locations, characterised by long-lasting developing soil. Our methodology enhanced the capability to compare greening trends on surfaces where soil had the possibility to develop up to 11–13 ka (EL) or up to 150 years (LR). Only Egesen–LIA (EL) areas, not exposed to active mass-wasting processes, can be assumed as an area retaining long-lasting developed soils and climax successions [37]. Such areas were also sensitive to the greening process driven by the ongoing climate change as underlined by the NDVI rise. The vegetative period in high-elevation sites at mid-latitude could, in fact, be extended due to the increasing temperature and to the shorter snow cover duration [79]. The tree species belonging to the treeline ecotone support the extension of the vegetative period, as demonstrated in other sectors of the European Alps (i.e., *Larix decidua* Mill. [80–83] and *Pinus cembra* L. [84–87]), whereas shrubs confirmed the shorter snow cover duration [79]. This implies a higher quantity of biomass in both non-alpine and alpine ecosystems, thus resulting in a higher NDVI index. The ongoing strong glacial retreat testifies that the climate warning enhanced at the highest elevation both on a global and a local scale [21,48,88–90]. The observed increasing NDVI values in the LR between the 1984 and the 2022 CE, but especially after 2011 CE, highlighted a major efficient colonisation by pioneer species and, therefore, the presence of a higher quantity of land-cover biomass, as also recorded in other proglacial areas [22,25,35].

6. Conclusions

The use of the Landsat time series, which combines long-term analysis with medium spatial resolution (30 m), can offer a useful tool for the characterisation of vegetation also in high mountain areas which are particularly affected by the ongoing climate warming. The recent deglaciation offers the opportunity for analysing the development of primary and secondary vegetation. The detection of greening in mountain areas using satellite data can be significantly improved by using geomorphological selection of deglaciated areas for which exposure times are known. This approach has improved the analysis of greening rates, which is usually carried out considering only land cover and altitude. The selection of deglaciated areas through landscape analysis improved the ability to isolate pixels characterised by similar topographic features (e.g., altitude and slope) and land cover types (e.g., bare rock and sparsely vegetated areas), but with different exposure times (e.g., different deglaciated areas). The known chronological constraint of deglaciated

areas allowed the comparison of land cover types in which soil processes had different timescales for soil development. The final observations highlighted an overall ongoing greening in the entire analysed area and underlined the necessity to apply specific pixel selection criteria for the trend analysis. The results showed, therefore, that the largest part of the study areas were affected by a significant greening process, with rates inversely associated with elevation (i.e., steeper rates were found at lower elevations). Such an observation was not confirmed by non-alpine bare rocks areas deglaciated since the Egesen (11–13 ka, i.e., EL_N). Preliminary inferences suggested the increase of vegetation covers or, at least, a more intense biomass accumulation of pioneering associations, although further analyses are required to quantitatively assess these observations. Our results did not reveal a strong land cover change that could imply a variation in terms of CORINE classification, as the greening degree is not sufficient to justify a new classification. However, considering the land cover types' spectral behaviour, the reflectance values underlined a general decrease in the different considered classes, comparing the 1990–1999 decade to the 2013–2022 CE period.

Supplementary Materials: The following supporting information can be downloaded at: https://www.mdpi.com/article/10.3390/rs15153847/s1, Figure S1: Number of analysed pixels grouped by deglaciated area and CORINE 1990 land cover class. Dark bars identify the total number of pixels; dots identify the median elevation of the pixel groups together with their standard deviation; Figure S2: Density distribution of surface reflectance values. Bands' names were standardised compliant with the Landsat 4–5 Thematic Mapper definition; Figure S3: Spatial distribution of the CORINE Land Cover classes[1] of the pixels comprised in 2400–2600 and 2800–3000 m a.s.l. elevation belts. Only pixels classified as "bare rocks" and "sparsely vegetated areas" in CLC90 were considered. All CORINE Land Cover published datasets were compared; Figure S4: Distribution of the CORINE Land Cover classes[1] of the pixels comprised in 2400–2600 and 2800–3000 m a.s.l. elevation belts. Only pixels classified as "bare rocks" and "sparsely vegetated areas" in CLC90 were considered. All CORINE Land Cover published datasets were compared.

Author Contributions: Conceptualisation, C.B., M.C.S., R.C. and S.G.; methodology, R.C. and S.G.; software, R.C. and S.G.; validation, C.B., M.C.S., R.C., R.S. (Roberto Salzano), R.S. (Rosamaria Salvatori) and S.G.; formal analysis, R.C., R.S. (Roberto Salzano) and S.G.; investigation, R.C. and S.G.; resources, C.B., M.C.S. and R.C.; data curation, C.B., M.C.S. and R.S. (Roberto Salzano); writing—original draft preparation, R.C., S.G. and R.S. (Roberto Salzano); writing—review and editing, C.B., M.C.S. and R.S. (Rosamaria Salvatori); visualization, R.C. and R.S. (Roberto Salzano); supervision, C.B. and M.C.S.; project administration, R.C.; funding acquisition, C.B. and M.C.S. All authors have read and agreed to the published version of the manuscript.

Funding: This research has been funded by Università di Pisa grant number PRA-2020_60, "La Terminazione I. Variazioni ambientali/paleoclimatiche intercorse nel periodo 25–11 ka.", P.I.: A. Ribolini; and "Fondi di Ateneo 2016–2019" of C.B. and M.C.S.

Data Availability Statement: Used data are accessible at https://earthexplorer.usgs.gov/ (accessed on 29 July 2023).

Acknowledgments: The authors thank Lena Rettori for English revision and spell-checking. The authors acknowledge the Research Infrastructures participating in the ITINERIS project with their Italian nodes: ACTRIS, ANAEE, ATLaS, CeTRA, DANUBIUS, DISSCO, e-LTER, ECORD, EMPHASIS, EMSO, EUFAR, Euro-Argo, EuroFleets, Geoscience, IBISBA, ICOS, JERICO, LIFEWATCH, LNS, N/R Laura Bassi, SIOS, SMINO. We wish to thank the Editor(s) and the four anonymous reviewers for their careful and valuable comments and suggestions, which allowed us to improve the manuscript.

Conflicts of Interest: The authors declare no conflict of interest. The funders had no role in the design of the study; in the collection, analyses, or interpretation of data; in the writing of the manuscript; or in the decision to publish the results.

Abbreviations

The following abbreviations are used in this manuscript:

CE	Common Era
EL_A	Egesen–LIA alpine (*sensu* [63]) deglaciated belt
EL_N	Egesen–LIA non-alpine (*sensu* [63]) deglaciated belt
ka	*kilo annum*
LIA	Little Ice Age
LR	LIA–Recent alpine (*sensu* [63]) deglaciated belt
NDVI	Normalized Difference Vegetation Index
OLI	Operational Land Imager
SCE	Snow Covered Extent
TM	Thematic Mapper

References

1. Intergovernmental Panel on Climate Change (IPCC). *Global Warming of 1.5 °C: IPCC Special Report on Impacts of Global Warming of 1.5 °C above Pre-Industrial Levels in Context of Strengthening Response to Climate Change, Sustainable Development, and Efforts to Eradicate Poverty*; Cambridge University Press: Cambridge, UK, 2022; p. 630. [CrossRef]
2. Intergovernmental Panel on Climate Change (IPCC). *The Ocean and Cryosphere in a Changing Climate: Special Report of the Intergovernmental Panel on Climate Change*; Cambridge University Press: Cambridge, UK, 2022; p. 1170. [CrossRef]
3. Intergovernmental Panel on Climate Change (IPCC). *Climate Change 2022—Impacts, Adaptation and Vulnerability: Working Group II Contribution to the Sixth Assessment Report of the Intergovernmental Panel on Climate Change*; Cambridge University Press: Cambridge, UK, 2023. [CrossRef]
4. Beniston, M.; Diaz, H.; Bradley, R. Climatic change at high elevation sites: An overview. *Clim. Chang.* **1997**, *36*, 233–251. [CrossRef]
5. Pepin, N.; Bradley, R.; Diaz, H.F.; Baraer, M.; Caceres, E.; Forsythe, N.; Fowler, H.; Greenwood, G.; Hashmi, M.; Liu, X.; et al. Elevation-dependent warming in mountain regions of the world. *Nat. Clim. Chang.* **2015**, *5*, 424–430. [CrossRef]
6. Böhm, R.; Auer, I.; Brunetti, M.; Maugeri, M.; Nanni, T.; Schöner, W. Regional temperature variability in the European Alps: 1760–1998 from homogenized instrumental time series. *Int. J. Climatol.* **2001**, *21*, 1779–1801. [CrossRef]
7. Auer, I.; Böhm, R.; Jurković, A.; Orlik, A.; Potzmann, R.; Schöner, W.; Ungersböck, M.; Brunetti, M.; Nanni, T.; Maugeri, M.; et al. A new instrumental precipitation dataset for the greater alpine region for the period 1800–2002. *Int. J. Climatol.* **2005**, *25*, 139–166. [CrossRef]
8. Brunetti, M.; Lentini, G.; Maugeri, M.; Nanni, T.; Auer, I.; Böhm, R.; Schöner, W. Climate variability and change in the Greater Alpine Region over the last two centuries based on multi-variable analysis. *Int. J. Climatol.* **2009**, *29*, 2197–2225. [CrossRef]
9. Sommer, C.; Malz, P.; Seehaus, T.C.; Lippl, S.; Zemp, M.; Braun, M.H. Rapid glacier retreat and downwasting throughout the European Alps in the early 21st century. *Nat. Commun.* **2020**, *11*, 3209. [CrossRef] [PubMed]
10. WGMS; NSIDC. World Glacier Inventory, Version 1. In *Technical Report*; World Glacier Monitoring Service: Boulder, CO, USA, 2012. [CrossRef]
11. Oerlemans, J. *Glaciers and Climate Change*; CRC Press, Tylor and Francis Group: Rotterdam, The Netherlands, 2001; p. 160.
12. Oerlemans, J. Extracting a Climate Signal from 169 Glacier Records. *Science* **2005**, *308*, 675–677. [CrossRef] [PubMed]
13. Zemp, M.; Frauenfelder, R.; Haeberli, W.; Hoelzle, M. Worldwide glacier mass balance measurements: General trends and first results of the extraordinary year 2003 in Central Europe. *Data Glaciol. Stud.* **2005**, *99*, 3–12.
14. Huss, M.; Bookhagen, B.; Huggel, C.; Jacobsen, D.; Bradley, R.; Clague, J.; Vuille, M.; Buytaert, W.; Cayan, D.; Greenwood, G.; et al. Toward mountains without permanent snow and ice. *Earth's Future* **2017**, *5*, 418–435. [CrossRef]
15. Intergovernmental Panel on Climate Change (IPCC). Information from Paleoclimate Archives. In *Climate Change 2013—The Physical Science Basis: Working Group I Contribution to the Fifth Assessment Report of the Intergovernmental Panel on Climate Change*; Cambridge University Press: Cambridge, UK, 2014; pp. 383–464. [CrossRef]
16. Jones, P.D.; Mann, M.E. Climate over past millennia. *Rev. Geophys.* **2004**, *42*, RG2002. [CrossRef]
17. Owens, M.J.; Lockwood, M.; Hawkins, E.; Usoskin, I.G.; Jones, G.S.; Barnard, L.; Schurer, A.; Fasullo, J. The Maunder minimum and the Little Ice Age: An update from recent reconstructions and climate simulations. *J. Space Weather Space Clim.* **2017**, *7*, A33. [CrossRef]
18. Baroni, C.; Casale, S.; Salvatore, M.C.; Ivy-Ochs, S.; Christl, M.; Carturan, L.; Seppi, R.; Carton, A. Double response of glaciers in the Upper Peio Valley (Rhaetian Alps, Italy) to the Younger Dryas climatic deterioration. *Boreas* **2017**, *46*, 783–798. [CrossRef]
19. Baroni, C.; Carton, A. Geomorphology of the upper Val di Genova (Adamello Group, Central Alps. *Geogr. Fis. Din. Quat.* **1996**, *19*, 3–17.
20. Ivy-Ochs, S.; Kerschner, H.; Maisch, M.; Christl, M.; Kubik, P.W.; Schlüchter, C. Latest Pleistocene and Holocene glacier variations in the European Alps. *Quat. Sci. Rev.* **2009**, *28*, 2137–2149. [CrossRef]

21. Zemp, M.; Frey, H.; Gärtner-Roer, I.; Nussbaumer, S.U.; Hoelzle, M.; Paul, F.; Haeberli, W.; Denzinger, F.; Ahlstrøm, A.P.; Anderson, B.M.; et al. Historically unprecedented global glacier decline in the early 21st century. *J. Glaciol.* **2015**, *61*, 745–762. [CrossRef]
22. Fischer, A.; Fickert, T.; Schwaizer, G.; Patzelt, G.; Groß, G. Vegetation dynamics in Alpine glacier forelands tackled from space. *Sci. Rep.* **2019**, *9*, 13918. [CrossRef]
23. Intergovernmental Panel on Climate Change (IPCC). *Climate Change and Land: An IPCC Special Report on Climate Change, Desertification, Land Degradation, Sustainable Land Management, Food Security, and Greenhouse Gas Fluxes in Terrestrial Ecosystems*; Cambridge University Press: Cambridge, UK, 2022; p. 896. [CrossRef]
24. Rumpf, S.B.; Gravey, M.; Brönnimann, O.; Luoto, M.; Cianfrani, C.; Mariethoz, G.; Guisan, A. From white to green: Snow cover loss and increased vegetation productivity in the European Alps. *Science* **2022**, *376*, 1119–1122. [CrossRef]
25. Gentili, R.; Baroni, C.; Panigada, C.; Rossini, M.; Tagliabue, G.; Armiraglio, S.; Citterio, S.; Carton, A.; Salvatore, M.C. Glacier shrinkage and slope processes create habitat at high elevation and microrefugia across treeline for alpine plants during warm stages. *Catena* **2020**, *193*, 104626. [CrossRef]
26. Global Climate Observing System (GCOS). *The Status of the Global Climate Observing System 2021: The GCOS Status Report (GCOS-240)*; World Meteorological Organization (WMO): Geneva, Switzerland, 2021; p. 384.
27. Potapov, P.; Hansen, M.C.; Pickens, A.; Hernandez-Serna, A.; Tyukavina, A.; Turubanova, S.; Zalles, V.; Li, X.; Khan, A.; Stolle, F.; et al. The Global 2000–2020 Land Cover and Land Use Change Dataset Derived From the Landsat Archive: First Results. *Front. Remote Sens.* **2022**, *3*, 856903. [CrossRef]
28. Hohensinner, S.; Atzler, U.; Fischer, A.; Schwaizer, G.; Helfricht, K. Tracing the Long-Term Evolution of Land Cover in an Alpine Valley 1820–2015 in the Light of Climate, Glacier and Land Use Changes. *Front. Environ. Sci.* **2021**, *9*, 683397. [CrossRef]
29. Wulder, M.A.; Roy, D.P.; Radeloff, V.C.; Loveland, T.R.; Anderson, M.C.; Johnson, D.M.; Healey, S.; Zhu, Z.; Scambos, T.A.; Pahlevan, N.; et al. Fifty years of Landsat science and impacts. *Remote Sens. Environ.* **2022**, *280*, 113195. [CrossRef]
30. Kumar, R.; Nath, A.J.; Nath, A.; Sahu, N.; Pandey, R. Landsat-based multi-decadal spatio-temporal assessment of the vegetation greening and browning trend in the Eastern Indian Himalayan Region. *Remote Sens. Appl. Soc. Environ.* **2022**, *25*, 100695. [CrossRef]
31. Verhoeven, V.B.; Dedoussi, I.C. Annual satellite-based NDVI-derived land cover of Europe for 2001–2019. *J. Environ. Manag.* **2022**, *302*, 113917. [CrossRef]
32. Filippa, G.; Cremonese, E.; Galvagno, M.; Isabellon, M.; Bayle, A.; Choler, P.; Carlson, B.Z.; Gabellani, S.; Morra di Cella, U.; Migliavacca, M. Climatic Drivers of Greening Trends in the Alps. *Remote Sens.* **2019**, *11*, 2527. [CrossRef]
33. Carlson, B.Z.; Corona, M.C.; Dentant, C.; Bonet, R.; Thuiller, W.; Choler, P. Observed long-term greening of alpine vegetation—A case study in the French Alps. *Environ. Res. Lett.* **2017**, *12*, 114006. [CrossRef]
34. Choler, P.; Bayle, A.; Carlson, B.Z.; Randin, C.; Filippa, G.; Cremonese, E. The tempo of greening in the European Alps: Spatial variations on a common theme. *Glob. Chang. Biol.* **2021**, *27*, 5614–5628. [CrossRef] [PubMed]
35. Knoflach, B.; Ramskogler, K.; Talluto, M.; Hofmeister, F.; Haas, F.; Heckmann, T.; Pfeiffer, M.; Piermattei, L.; Ressl, C.; Wimmer, M.H.; et al. Modelling of Vegetation Dynamics from Satellite Time Series to Determine Proglacial Primary Succession in the Course of Global Warming—A Case Study in the Upper Martell Valley (Eastern Italian Alps). *Remote Sens.* **2021**, *13*, 4450. [CrossRef]
36. Marazzi, S. *Atlante Orografico delle Alpi: SOIUSA: Suddivisione Orografica Internazionale Unificata del Sistema Alpino*; Quaderni di Cultura Alpina; Priuli & Verlucca: Pavone Canavese, Italy, 2005; p. 416.
37. Baroni, C.; Gennaro, S.; Salvatore, M.C.; Ivy-Ochs, S.; Christl, M.; Cerrato, R.; Orombelli, G. Last Lateglacial glacier advance in the Gran Paradiso Group reveals relatively drier climatic conditions established in the Western Alps since at least the Younger Dryas. *Quat. Sci. Rev.* **2021**, *255*, 106815. [CrossRef]
38. Salvatore, M.C.; Zanoner, T.; Baroni, C.; Carton, A.; Banchieri, F.A.; Viani, C.; Giardino, M.; Perotti, L. The state of Italian glaciers: A snapshot of the 2006–2007 hydrological period. *Geogr. Fis. Din. Quat.* **2015**, *38*, 175–198. [CrossRef]
39. Gennaro, S. Glaciers of the Gran Paradiso Group as Indicator of Lateglacial and Holocene Climatic Changes in the Western Alps. Ph.D. Thesis, University of Pisa, Pisa, Italy, 2020.
40. Le Bayon, B.; Ballèvre, M. Deformation history of a subducted continental crust (Gran Paradiso, Western Alps): Continuing crustal shortening during exhumation. *J. Struct. Geol.* **2006**, *28*, 793–815. [CrossRef]
41. Dal Piaz, G.V.; Gianotti, F.; Monopoli, B.; Pennacchioni, G.; Tartarotti, P.; Schiavo, A. *Carta Geologica d'Italia alla Scala 1:50,000 e Note Illustrative. Foglio 91 Chatillon*; ISPRA—Istituto Superiore per la Protezione e la Ricerca Ambientale: Rome, Italy, 2008; p. 153.
42. Beltrando, M.; Compagnoni, R.; Lombardo, B. (Ultra-) High-pressure metamorphism and orogenesis: An Alpine perspective. *Gondwana Res.* **2010**, *18*, 147–166. [CrossRef]
43. Polino, R.; Bonetto, F.; Carraro, F.; Gianotti, F.; Gouffon, Y.; Malusà, M.; Martin, S.; Perello, P.; Schiavo, A. *Carta Geologica d'Italia alla Scala 1:50,000 e Note Illustrative. Foglio 90 Aosta*; ISPRA—Istituto Superiore per la Protezione e la Ricerca Ambientale: Rome, Italy, 2015; p. 148.
44. Elter, G. *Carte Géologique de la Vallée d'Aoste, Échelle 1:100.000 [Geological Map of the Aosta Valley]*; C.N.R. Centro di studio sui problemi dell'Orogeno delle Alpi occidentali, Torino. S.E.L.C.A.: Firenze, Italy, 1987.
45. Gasco, I.; Gattiglio, M.; Borghi, A. Structural evolution of different tectonic units across the Austroalpine–Penninic boundary in the middle Orco Valley (Western Italian Alps). *J. Struct. Geol.* **2009**, *31*, 301–314. [CrossRef]

46. Manzotti, P.; Le Carlier De Veslud, C.; Le Bayon, B.; Ballèvre, M. Petro-structural map of the Money Unit (Gran Paradiso Massif, Valnontey valley, Western Alps). *J. Maps* **2014**, *10*, 324–340. [CrossRef]
47. Piana, F.; Fioraso, G.; Irace, A.; Mosca, P.; D'Atri, A.; Barale, L.; Falletti, P.; Monegato, G.; Morelli, M.; Tallone, S.; et al. Geology of Piemonte region (NW Italy, Alps–Apennines interference zone). *J. Maps* **2017**, *13*, 395–405. [CrossRef]
48. Salvatore, M.C.; Bertocchini, N.; Gennaro, S.; Baroni, C. Geomorphological Map of Valnontey (Gran Paradiso Group, Western Alps, Italy). *Geogr. Fis. Din. Quat.* **2021**, *44*, 197–213. [CrossRef]
49. Peel, M.; Finlayson, B.; McMahon, T. Updated world map of the Köppen-Geiger climate classification. *Hydrol. Earth Syst. Sci.* **2007**, *11*, 1633–1644. [CrossRef]
50. Beck, H.E.; Zimmermann, N.E.; McVicar, T.R.; Vergopolan, N.; Berg, A.; Wood, E.F. Present and future Köppen-Geiger climate classification maps at 1-km resolution. *Sci. Data* **2018**, *5*, 180214. [CrossRef] [PubMed]
51. Isotta, F.A.; Frei, C.; Weilguni, V.; Perčec Tadić, M.; Lassègues, P.; Rudolf, B.; Pavan, V.; Cacciamani, C.; Antolini, G.; Ratto, S.M.; et al. The climate of daily precipitation in the Alps: Development and analysis of a high-resolution grid dataset from pan-Alpine rain-gauge data. *Int. J. Climatol.* **2014**, *34*, 1657–1675. [CrossRef]
52. Brunetti, M.; Maugeri, M.; Monti, F.; Nanni, T. Temperature and precipitation variability in Italy in the last two centuries from homogenised instrumental time series. *Int. J. Climatol.* **2006**, *26*, 345–381. [CrossRef]
53. European Environment Agency (EEA). *Regional Climate Change and Adaptation: The Alps Facing the Challenge of Changing Water Resources*; EEA: Copenhagen, Denmark, 2009; p. 148. [CrossRef]
54. Brunetti, M.; Maugeri, M.; Nanni, T.; Simolo, C.; Spinoni, J. High-resolution temperature climatology for Italy: Interpolation method intercomparison. *Int. J. Climatol.* **2014**, *34*, 1278–1296. [CrossRef]
55. Poussin, C.; Guigoz, Y.; Palazzi, E.; Terzago, S.; Chatenoux, B.; Giuliani, G. Snow Cover Evolution in the Gran Paradiso National Park, Italian Alps, Using the Earth Observation Data Cube. *Data* **2019**, *4*, 138. [CrossRef]
56. Harris, I.; Osborn, T.J.; Jones, P.; Lister, D. Version 4 of the CRU TS monthly high-resolution gridded multivariate climate dataset. *Sci. Data* **2020**, *7*, 109. [CrossRef] [PubMed]
57. Raffl, C.; Mallaun, M.; Mayer, R.; Erschbamer, B. Vegetation succession pattern and diversity changes in a Glacier Valley, Central Alps, Austria. *Arct. Antarct. Alp. Res.* **2006**, *38*, 421–428. [CrossRef]
58. Hoffmann, S.; Steiner, L.; Schweiger, A.H.; Chiarucci, A.; Beierkuhnlein, C. Optimizing sampling effort and information content of biodiversity surveys: A case study of alpine grassland. *Ecol. Inform.* **2019**, *51*, 112–120. [CrossRef]
59. Mainetti, A.; D'Amico, M.; Probo, M.; Quaglia, E.; Ravetto Enri, S.; Celi, L.; Lonati, M. Successional Herbaceous Species Affect Soil Processes in a High-Elevation Alpine Proglacial Chronosequence. *Front. Environ. Sci.* **2021**, *8*, 615499. [CrossRef]
60. Vanuzzo, C. The glacier retreat in Valle D'Aosta (Western Italian Alps) from the Little Ice Age to the second half of the 20th century: Linear, areal, volumetric and equilibrium line altitude changes. *Geogr. Fis. Din. Quat.* **2001**, *24*, 99–113.
61. Baroni, C.; Salvatore, M.C.; Alderighi, L.; Gennaro, S.; Zanoner, T.; Carton, A.; Carturan, L.; Zorzi, M.; Giardino, M.; Bertotto, S.; et al. The changing Italian glaciers. In *NextData Project Final Volume—Climate and Environmental Changes in the Italian Mountains*; Donato, A., Palazzi, E., Eds.; CNR–IGG: Pisa, Italy, 2019; Chapter 8, p. 272.
62. Baroni, C.; Salvatore, M.C.; Alderighi, L.; Gennaro, S. Italian glaciers, sensitive sentinels of climate change. In *The Researches of the University of Pisa in the Field of the Effects of Climate Change*. *Agrochimica*; Lorenzini, G., Ed.; Pisa University Press: Pisa, Italy, 2019; pp. 213–220.
63. Testolin, R.; Attorre, F.; Jiménez-Alfaro, B. Global distribution and bioclimatic characterization of alpine biomes. *Ecography* **2020**, *43*, 779–788. [CrossRef]
64. Kriegler, F.J.; Malila, W.A.; Nalepka, R.; Richardson, W. Preprocessing transformations and their effects on multispectral recognition. In Proceedings of the Sixth International Symposium on Remote Sensing of Environment, Ann Arbor, MI, USA, 13–16 October 1969; pp. 97–131.
65. Gates, D.M. *Biophysical Ecology*; Springer: New York, NY, USA, 1980; p. 611.
66. Baldridge, A.; Hook, S.; Grove, C.; Rivera, G. The ASTER spectral library version 2.0. *Remote Sens. Environ.* **2009**, *113*, 711–715. [CrossRef]
67. Meerdink, S.K.; Hook, S.J.; Roberts, D.A.; Abbott, E.A. The ECOSTRESS spectral library version 1.0. *Remote Sens. Environ.* **2019**, *230*, 111196. [CrossRef]
68. Salvatori, R.; Salzano, R.; Valt, M.; Cerrato, R.; Ghergo, S. The Collection of Hyperspectral Measurements on Snow and Ice Covers in Polar Regions (SISpec 2.0). *Remote Sens.* **2022**, *14*, 2213. [CrossRef]
69. Kokaly, R.F.; Clark, R.N.; Swayze, G.A.; Livo, K.E.; Hoefen, T.M.; Pearson, N.C.; Wise, R.A.; Benzel, W.M.; Lowers, H.A.; Driscoll, R.L.; et al. Spectral Library Version 7. In *Technical Report*; USGS: Reston, VA, USA, 2017. [CrossRef]
70. Unger, S.; Vargas, S.; May, J.; Oberbauer, S. Arctic Moss Spectral Reflectance Desiccation Experiment From Samples Collected in Northern Alaska. Data Set. From the Ecological Spectral Information System (EcoSIS). Available online: http://ecosis.org (accessed on 29 July 2023).
71. Lamchin, M.; Lee, W.K.; Jeon, S.W.; Wang, S.W.; Lim, C.H.; Song, C.; Sung, M. Long-term trend and correlation between vegetation greenness and climate variables in Asia based on satellite data. *Sci. Total Environ.* **2018**, *618*, 1089–1095. [CrossRef]
72. Lamchin, M.; Wang, S.W.; Lim, C.H.; Ochir, A.; Pavel, U.; Gebru, B.M.; Choi, Y.; Jeon, S.W.; Lee, W.K. Understanding global spatio-temporal trends and the relationship between vegetation greenness and climate factors by land cover during 1982–2014. *Glob. Ecol. Conserv.* **2020**, *24*, e01299. [CrossRef]

73. Cohen, J.; Cohen, P.; West, S.G.; Aiken, L.S. *Applied Multiple Regression/Correlation Analysis for the Behavioral Sciences*, 3rd ed.; Routledge: New York, NY, USA, 2002; p. 536. [CrossRef]
74. Wan, K.X.; Vidavsky, I.; Gross, M.L. Comparing similar spectra: From similarity index to spectral contrast angle. *J. Am. Soc. Mass Spectrom.* **2002**, *13*, 85–88. [CrossRef]
75. R Core Team. *R: A Language and Environment for Statistical Computing*; R Foundation for Statistical Computing: Vienna, Austria, 2022. Available online: https://www.R-project.org/ (accessed on 29 July 2023).
76. Filippa, G.; Cremonese, E.; Galvagno, M.; Bayle, A.; Choler, P.; Bassignana, M.; Piccot, A.; Poggio, L.; Oddi, L.; Gascoin, S.; et al. On the distribution and productivity of mountain grasslands in the Gran Paradiso National Park, NW Italy: A remote sensing approach. *Int. J. Appl. Earth Obs. Geoinf.* **2022**, *108*, 102718. [CrossRef]
77. Cannone, N.; Sgorbati, S.; Guglielmin, M. Unexpected impacts of climate change on alpine vegetation. *Front. Ecol. Environ.* **2007**, *5*, 360–364. [CrossRef]
78. Huang, K.; Zu, J.; Zhang, Y.; Cong, N.; Liu, Y.; Chen, N. Impacts of snow cover duration on vegetation spring phenology over the Tibetan Plateau. *J. Plant Ecol.* **2019**, *12*, 583–592. [CrossRef]
79. Carrer, M.; Dibona, R.; Prendin, A.L.; Brunetti, M. Recent waning snowpack in the Alps is unprecedented in the last six centuries. *Nat. Clim. Chang.* **2023**, *13*, 155–160. [CrossRef]
80. Cerrato, R.; Salvatore, M.C.; Brunetti, M.; Coppola, A.; Baroni, C. Dendroclimatic relevance of "Bosco Antico", the most ancient living European larch wood in the Southern Rhaetian Alps (Italy). *Geogr. Fis. Din. Quat.* **2018**, *41*, 35–49. [CrossRef]
81. Coppola, A.; Leonelli, G.; Salvatore, M.C.; Pelfini, M.; Baroni, C. Tree-ring- Based summer mean temperature variations in the Adamello-Presanella Group (Italian Central Alps), 1610–2008 AD. *Clim. Past* **2013**, *9*, 211–221. [CrossRef]
82. Leonelli, G.; Coppola, A.; Baroni, C.; Salvatore, M.C.; Maugeri, M.; Brunetti, M.; Pelfini, M. Multispecies dendroclimatic reconstructions of summer temperature in the European Alps enhanced by trees highly sensitive to temperature. *Clim. Chang.* **2016**, *137*, 275–291. [CrossRef]
83. Leonelli, G.; Coppola, A.; Salvatore, M.C.; Baroni, C.; Battipaglia, G.; Gentilesca, T.; Ripullone, F.; Borghetti, M.; Conte, E.; Tognetti, R.; et al. Climate signals in a multispecies tree-ring network from central and southern Italy and reconstruction of the late summer temperatures since the early 1700s. *Clim. Past* **2017**, *13*, 1451–1471. [CrossRef]
84. Carrer, M.; Nola, P.; Edouard, J.L.; Motta, R.; Urbinati, C. Regional variability of climate growth relationships in Pinus cembra high elevation forests in the Alps. *J. Ecol.* **2007**, *95*, 1072–1083. [CrossRef]
85. Cerrato, R.; Salvatore, M.C.; Gunnarson, B.E.; Linderholm, H.W.; Carturan, L.; Brunetti, M.; De Blasi, F.; Baroni, C. A *Pinus cembra* L. tree-ring record for late spring to late summer temperature in the Rhaetian Alps, Italy. *Dendrochronologia* **2019**, *53*, 22–31. [CrossRef]
86. Saulnier, M.; Edouard, J.L.; Corona, C.; Guibal, F. Climate/growth relationships in a *Pinus cembra* high-elevation network in the Southern French Alps. *Ann. For. Sci.* **2011**, *68*, 189–200. [CrossRef]
87. Cerrato, R.; Salvatore, M.C.; Carrer, M.; Brunetti, M.; Baroni, C. Blue intensity of Swiss stone pine as a high-frequency temperature proxy in the Alps. *Eur. J. For. Res.* **2023**, *142*, 933–948. [CrossRef]
88. Baroni, C.; Bondesan, A.; Carturan, L.; Chiarle, M. Annual glaciological survey of Italian Glaciers (2019). *Geogr. Fis. Din. Quat.* **2020**, *43*, 45–142.
89. Carturan, L.; Rastner, P.; Paul, F. On the disequilibrium response and climate change vulnerability of the mass-balance glaciers in the Alps. *J. Glaciol.* **2020**, *66*, 1034–1050. [CrossRef]
90. Hugonnet, R.; McNabb, R.; Berthier, E.; Menounos, B.; Nuth, C.; Girod, L.; Farinotti, D.; Huss, M.; Dussaillant, I.; Brun, F.; et al. Accelerated global glacier mass loss in the early twenty-first century. *Nature* **2021**, *592*, 726–731. [CrossRef]